DIRECT NUMERICAL SIMULATIONS OF VARIABLE-ASPECT-RATIO TURBULENT DUCT FLOWS AT LOW TO MODERATE REYNOLDS NUMBERS

Ricardo Vinuesa
MMAE Department
Illinois Institute of Technology
Chicago, IL 60616, USA
rvinuesa@hawk.iit.edu

Azad Noorani
Linné FLOW Centre
KTH Mechanics
O. Backe 18, Stockholm, Sweden
azad@mech.kth.se

Adrián Lozano-Durán
School of Aeronautics
Universidad Politécnica de Madrid
28040 Madrid, Spain
adrian@torroja.dmt.upm.es

George El Khoury
Linné FLOW Centre
KTH, Sweden
georgeek@mech.kth.se

Philipp Schlatter
Linné FLOW Centre
KTH, Sweden
pschlatt@mech.kth.se

Paul F. Fischer
MCS, ANL
Argonne, USA
fischer@mcs.anl.gov

Hassan M. Nagib
MMAE Department
IIT, Chicago, USA
nagib@iit.edu

ABSTRACT

Three-dimensional effects in turbulent duct flows, i.e., side-wall boundary layers and secondary motions, are studied by means of direct numerical simulations (DNS). The spectral element code Nek5000 is used to compute turbulent duct flows with aspect ratios 1 to 7 (at $Re_{b,c} = 2800$, $Re_\tau \simeq 180$) and 1 (at $Re_{b,c} = 5600$, $Re_\tau \simeq 330$) in streamwise-periodic boxes of length $25h$. The total number of grid points ranges from 28 to 145 million, and the fluid kinematic viscosity ν was adjusted iteratively in order to keep the same bulk Reynolds number at the centerplane with changing aspect ratio. Spanwise variations in wall shear, mean-flow profiles and turbulence statistics are analyzed with aspect ratio, and also compared with the 2D channel. These computations show good agreement with experimental measurements carried out at IIT in parallel, and reinforces one important conclusion: the conditions obtained in the core region of a high-aspect-ratio duct cannot exactly be reproduced by spanwise-periodic DNSs of turbulent channel flows.

MOTIVATING PROBLEM

The flow of fluids in ducts with rectangular cross-section is frequently encountered in a variety of environmental, technical and even biological applications. Typical examples of duct flows can be found in urban drainage systems, ventilation systems and combustion engines. In addition, rectangular duct flows with different width-to-height ratios serve as a great platform to study the impact of three-dimensional effects on flow properties which are relevant from a design perspective, such as wall shear, pressure drop, etc. Accordingly, the understanding of flow physics in such situations has a direct and substantial impact on everyday life, and an adequate knowledge of such flow problem will help in finding scientific methods to reduce drag and the like. One of the goals of the present study is to help elucidate one particular aspect of turbulence, namely near-wall turbulence in ducts, i.e., when a secondary flow (as defined by Prandtl (1926)) is present. In general, near-wall turbulent structures in wall-bounded shear flows primarily scale in terms of the so-scaled viscous length scale (defined below), which might be very small as the Reynolds number Re is increased. However, according to recent experimental studies (Guala et al. (2006) and Monty et al. (2007)), very large-scale motions with lengths of $5h$ up to $20h$ are found in fully-developed turbulent duct and pipe flows (h being the duct half-height or pipe radius, respectively). These structures, being strongest in the outer region, extend throughout the overlap layer and even leave their footprint quite close to the wall. Large-scale motions thus play an important role in the dynamics of turbulent duct flows.

Another important implication of rectangular duct flows is the fact that they allow us to study secondary flows in relatively simple geometries. Secondary flows are also present in more complicated geometries used in engineering applications, such as diffusers, turbine blades or wings, but their actual impact on flow physics is largely unknown. In fact, industrial computations of these flows are mainly based on Reynolds Averaged Navier Stokes (RANS) simulations, where turbulence is modeled relying on largely empirical arguments. Therefore, another important goal of the present project is to understand the influence of three-dimensional effects on near-wall turbulence, in order to provide engineers and model developers accurate information to improve currently available RANS models. In addition, we also compare results from our duct flow computations with recent experimental work carried out at the Illinois Institute of Technology (Vinuesa, 2013). The final goal is to combine experimental and computational data to estimate the so-called von Kármán coefficient κ for high-aspect-ratio duct flows, which is another important parameter used in the formulation of RANS models. In fact, the value of κ is directly related to wall shear, thus the importance of accurately determining this parameter in order to improve skin friction predictions.

Three-dimensional effects present in turbulent duct flows

Two mechanisms present in the duct are responsible for three-dimensional effects: the boundary layers growing along the side-walls of the duct, and the secondary motions produced at the duct corners. Despite the wide range of available DNS data for channel flows (del Álamo et al., 2004; Jiménez et al., 2004; Moser et al., 1999), all these simulations were carried out assuming periodicity of the domain in the streamwise (x) and spanwise (z) directions. Whereas the first assumption implies that the flow is fully-developed in x, the second one leads to a homogeneous channel in z. As discussed by Vinuesa (2013), the two previously mentioned effects (not captured by the z-periodic channel) lead to different skin friction predictions at the core of the duct, that do not agree with the periodic channel.

In an experimental duct flow, the first three-dimensional effect influencing the physics at the core is the growth of the boundary layers located at the side-walls. Their growth leads to increased momentum in the core of the flow, which eventually increases the measured wall shear along the bottom plate. The other three-dimensional effect present in the experimental duct is the secondary flow, i.e., the cross-flow field in the $y-z$ plane, normal to the streamwise direction x. Here we will focus on the effect of the secondary motions of Prandtl's second kind, which are associated with the secondary Reynolds shear stress $\overline{vw}$ and the anisotropy of the cross-stream Reynolds stress $\overline{v^2}-\overline{w^2}$; e.g., see Moinuddin et al. (2004). It is important to note that the secondary flows of the second kind are entirely due to turbulence, and are absent in laminar flows. The secondary motions consist of eight streamwise vortices, two counter-rotating in each corner, with the flow directed toward the corners. Although this kind of secondary flow is relatively weak (about 2-3% of the bulk velocity (Huser and Biringen, 1993)), its effect on the mean velocity distribution is important: they convect mean velocity from the walls towards regions around the corner bisectors. This reduced mean velocity near the wall actually leads to a reduced wall shear stress value.

Although the measurements by Vinuesa (2013) showed a relationship between skin friction and aspect ratio, it was difficult to independently analyze the two factors responsible for this effect due to experimental limitations. Numerical simulations are, in principle, able to provide data accessible at any point of the domain, without the constraints of probe size and experimental design. Therefore, we carried out direct numerical simulations of turbulent duct flows at moderate Reynolds numbers with several aspect ratio configurations (as described in the following section), with the aim of assessing these three-dimensional effects. In addition to achieving a better understanding of the mechanisms leading to the change in skin friction with AR, the proposed simulations substantially enrich the currently limited database of turbulent duct flows available in the literature. The most extensive numerical studies are the DNSs by Uhlmann et al. (2007) and Pinelli et al. (2009) at Re_τ values up to 300 and Huser and Biringen (1993) at $Re_\tau = 300$, all of them for square ducts. It is important to note that most of these simulations were performed in short computational boxes, on the order of 1/4 the length considered in the present study.

DESCRIPTION OF THE NUMERICAL SIMULATIONS

The DNSs considered in the present study were carried out on the Cray XE6 machine "Lindgren" at the PDC Center from KTH in Stockholm (Sweden), the Blue Gene/P machine "Intrepid" at the ALCF from Argonne National Laboratory in Chicago (USA), and the Cray XT5 machine "Louhi" at the CSCIT Center for Science in Espoo (Finland). They required from 2048 to 16384 cores, and MPI was employed for parallelization.

The code chosen for this project is Nek5000, developed by Fischer et al. (2008) at the Argonne National Laboratory (nek5000.mcs.anl.gov), and based on the spectral element method (SEM), originally proposed by Patera (1984). In this code, the governing equations (incompressible Navier-Stokes in our case) are cast in weak form, so they are multiplied by a test function and integrated over the domain. The spatial discretization is done by means of the Galerkin approximation, following the $\mathbb{P}_N - \mathbb{P}_{N-2}$ formulation, where the pressure is associated with polynomials two degrees lower than the velocity. The velocity space is of Nth-order Lagrange polynomial interpolants $h_i^N(x)$, based on tensor-product arrays of Gauss-Lobatto-Legendre (GLL) quadrature points on each local element Ω^e, $e = 1,\ldots,E$. If $\varepsilon_j^N \in [-1,1]$ denotes one of the $(N+1)$ GLL quadrature points and δ_{ij} is the Kronecker delta, the condition $h_i^N\left(\varepsilon_j^N\right) = \delta_{ij}$ is satisfied. Thus, the three-dimensional velocity vector is interpolated within a spectral element by means of three Lagrange polynomials of order N.

All the DNSs of turbulent duct flows were carried out in computational boxes of streamwise length $L_x = 25h$ (where h is the duct half-height), which are long enough to capture the longest streamwise turbulent structures according to experimental measurements in pipe flow (Guala et al., 2006) and DNSs of turbulent channel flows (Jiménez and Hoyas, 2010). Periodicity was considered in the streamwise direction, which involves fully-developed flow. Therefore, spectral elements were distributed uniformly along x, and their spacing was chosen so that $\Delta x^+_{\max} < 10$. The wall-normal length was $L_y = 2h$ in all the cases, whereas the spanwise length L_z was set to yield the slightly different aspect ratios under consideration. The mesh in the nonhomogeneous directions (y and z) was designed so that the maximum spacing $\Delta y^+_{\max}$ is below 5 wall units, and we have at least 4 grid points below $y^+ = 1$. In these two directions, the spectral elements were located according to the Gauss-Lobatto-Chebyshev distribution close to the wall, and using a uniform distribution at the core region. Those two were blended respecting the two previous restrictions and not exceeding the growth of the Kolmogorov scale.

Another aspect of this computational campaign was to study in detail the dependence of the centerplane duct conditions with aspect ratio, and to connect experimental and numerical results. In the experiment by Vinuesa (2013), the centerline velocity U_c was kept constant for the different aspect ratios by using a PID controller which regulated the mass flow accordingly. Here, we replicated that approach through the following iterative process: in Nek5000, the pressure gradient is adjusted after each time-step in order to obtain a fixed bulk velocity over the section $U_b = 1$. As an input to the simulation, one provides the bulk Reynolds number $Re_b = U_b h/\nu$, which essentially is equivalent to providing the kinematic viscosity ν since h is the length scale. However, we do not want to fix the cross-sectional bulk velocity, but the centerplane bulk velocity $U_{b,c}$ instead.

Therefore, we used preliminary runs to iteratively adjust the input Re_b necessary for obtaining certain target centerplane Reynolds numbers $Re_{b,c}$, in our case 2800 and 5600 (which, for channel flows, would correspond to $Re_\tau \simeq 180$ and 330 respectively). Doing so, the input Re_b were used on the final runs with nominally the same Reynolds number at the centerplane, and therefore variations in local friction (U_c^+ and $Re_{\tau,c}$) are uniquely due to aspect ratio effects. All the duct cases under consideration are summarized in Table 1. Interpolation order $N = 11$ was considered for all the cases, although the flow was allowed to approach a fully turbulent state by means of preliminary runs with interpolation orders $N = 5$ and 7. The initial profile was a laminar duct flow expansion with a wall-normal volume force tripping (active only during the initial $N = 5$ runs) analogous to the one used in the spatially developing boundary layer simulation by Schlatter and Örlü (2012).

Table 1. Summary of turbulent duct flow cases computed in the present study.

AR	$Re_{\tau,c}$	Re_b	$Re_{b,c}$	Grid-points
1	178	2500	2796	28 million
3	178	2581	2786	62 million
5	176	2592	2775	96 million
7	174	2575	2737	130 million
1	323	5086	5604	145 million

The random volume force tripping defined by Schlatter and Örlü (2012) consists of a spanwise line disturbance with amplitude, spanwise length scale and temporal frequency depending on the particular cases. This disturbance is located along the streamwise center of the box (around $x \simeq 12h$), and emulates experimental tripping conditions. Figures 1 shows the turbulent field of the aspect ratio 3 case, with $Re_{b,c} \simeq 2800$, at convective times of 20 and 60 (where time non-dimensionalization is done in terms of bulk velocity U_b and duct half-height h). In this simulation, runs between 0 and 50 convective time units were done with $N = 5$ and tripping activated, between 50 and 100 with $N = 7$ and tripping disabled, and after 100 time units the interpolation order was increased to $N = 11$. It is interesting to observe how the breakdown from the initial laminar profile extends to the whole field, eventually leading to a self-sustained turbulent process which does not require forcing anymore.

SKIN FRICTION RESULTS

The three-dimensional effects present in the duct, and not captured by the channel simulations, are responsible for two energy fluxes impacting the flow at the duct centerplane: first, the side-wall boundary layers accelerate the core of the duct, thus injecting energy at the centerplane, leading to higher wall shear. Second, the secondary motions of Prandtl's second kind convect mean velocity from the near-wall region at the core of the duct, extracting energy from the centerplane to dissipate it at the corner bisectors, therefore reducing wall shear. This is shown in Figure 2, which presents $U_c^+ = U_c/u_\tau$ values obtained from the DNSs discussed here for the various aspect ratio cases, compared with reference channel flow data by del Álamo et al. (2004) (note that the $Re_\tau \simeq 330$ channel value was obtained through interpolation). The first important observation inferred from this figure is the fact that aspect ratio 3 exhibits higher skin friction than aspect ratio 1. However, aspect ratio 5 shows lower skin friction than 3, and the next case (AR = 7) shows a wall shear value slightly lower. The latter trend is the expected behavior which can also be observed in experiments (Vinuesa, 2013): larger aspect ratios produce lower skin friction at the core because the influence of the side-wall boundary layers is less important, i.e., the energy injected at the core is lower. Nevertheless, this trend is reversed for low aspect ratios, so the role of the secondary motions has to be analyzed too. Figure 3 shows the cross-flow velocity magnitude $\sqrt{V^2 + W^2}$ and the in-plane streamlines for the aspect ratios 3 computed with $Re_{\tau,c} \simeq 180$ and the aspect ratio 1 at $Re_{\tau,c} \simeq 330$. As discussed in Vinuesa (2013), the side-wall boundary layers increase their thickness from h to around $2.85h$, thus injecting more energy in the core of the duct, which cannot be evacuated by the secondary motions at the corners. Note that the boundary layer thickness δ_z was evaluated as the spanwise location z at which $\mathrm{d}U^+/\mathrm{d}z^+ = 0$. The streamlines show how the mean streamwise vortices along the top and bottom walls start to stretch in the spanwise direction, but the increased energy at the centerplane produces larger wall shear. In the aspect ratio 5 case, the side-wall boundary layers would be $4.25h$ thick, and the number of secondary vortices increases significantly. This facilitates the evacuation of the extra energy transmitted to the duct core, which explains why the skin friction from aspect ratio 5 decreases. It is also discussed by Vinuesa (2013) how the boundary layers at the side-walls increase their size again to $5.95h$ in the aspect ratio 7 case, but correspondingly the amount of energy evacuated by the secondary vortices also increases due to increased number of vortices involved in the process. It is important to note that, whereas in the AR = 3 case the δ_z represents around 95% of the half-width, for aspect ratios 5 and 7 this percentage is about 85%. This means that, even if δ_z still increases from AR = 5 to 7, the ratio δ_z/w (where w is the duct half-width) reaches a constant value of 0.85. In other words, the AR = 3 case reflects the fact that the side-wall boundary layers grow faster than the rate of formation of streamwise vortices, therefore wall shear increases. This is what we call the "low-AR" trend. However, for aspect ratios of 5 and larger, the side-wall boundary layer length divided by half-width reaches its maximum, whereas the number of secondary vortices still increases. This explains why, in the "large-AR" trend, wall shear is reduced with aspect ratio. This behavior is expected to balance for very large aspect ratios, of 24 and larger, as can be inferred from experimental measurements (Vinuesa, 2013). This would mean that the energy fluxes (towards the centerplane, introduced by the side-wall boundary layers of size $\delta_z \simeq 0.85w$, and from the core, extracted by a number of secondary vortices) balance each other. The extent of the side-wall boundary layers, and the formation of the array of secondary vortices along the bottom wall have not been discussed in the literature before, although Monty in his PhD work conjectured about the existence of such an array of vortices.

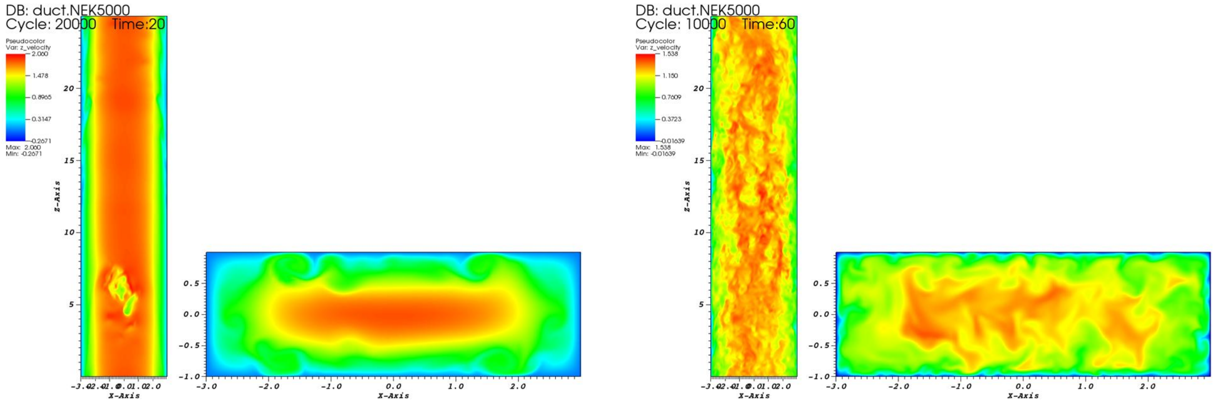

Figure 1. Turbulent field of the aspect ratio 3 case with $Re_{\tau,c} \simeq 180$, after 20 (left) and 60 (right) convective time units from start of the simulation. The left figure has interpolation order $N = 5$ and tripping is enabled, whereas for the right figure $N = 7$ and no tripping was considered. Streamwise velocity is plotted on both figures; for each figure, the flow goes from bottom to top on the left panel, and is outgoing on the right one.

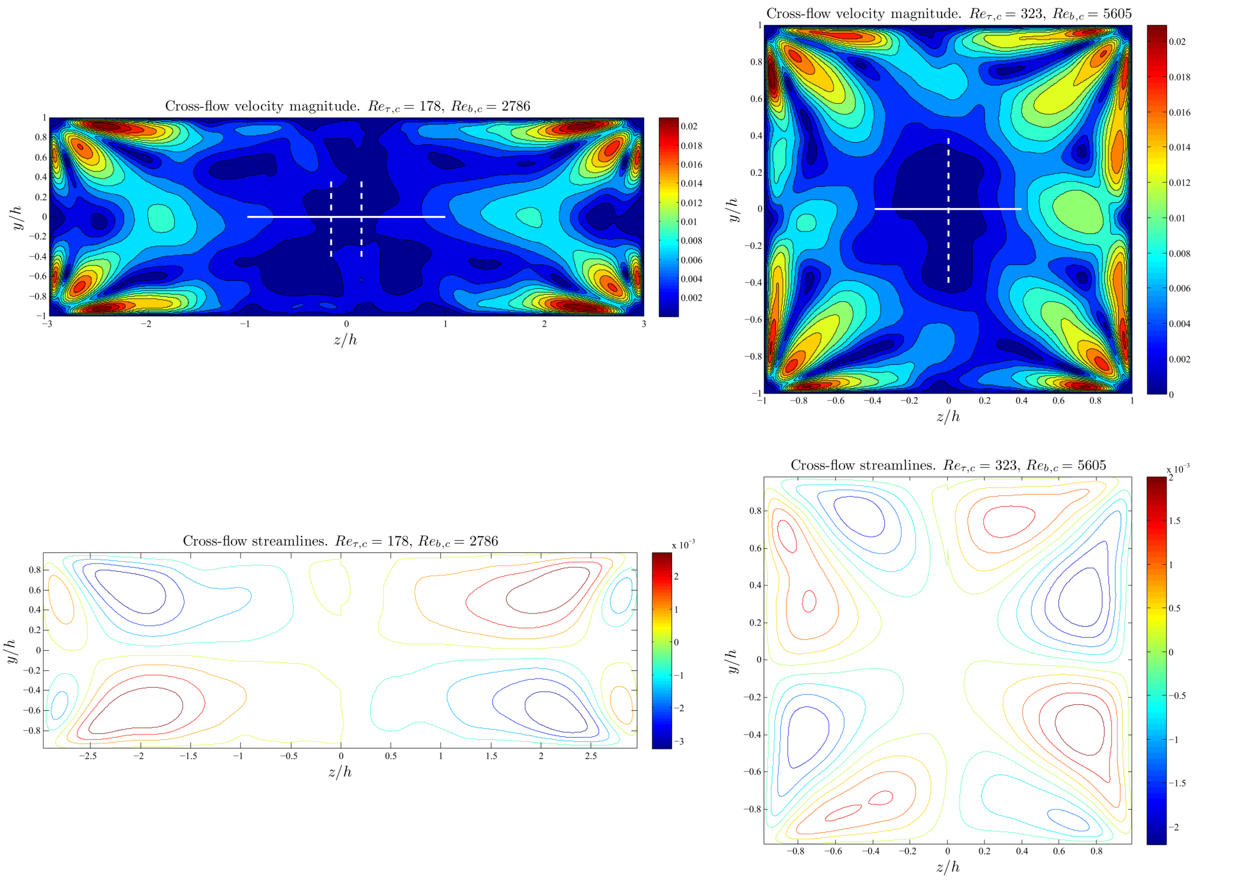

Figure 3. Cross-flow velocity magnitude $\sqrt{V^2+W^2}$ (top) and contours of the streamfunction (bottom) for the AR $= 3$ duct case computed at $Re_{\tau,c} \simeq 180$ (left) and the AR $= 1$ duct case with $Re_{\tau,c} \simeq 330$. Solid white lines represent the upper and lower boundary layer thicknesses at $z = 0$, $\delta_y \simeq h$. Dashed white lines show the side-wall boundary layer thicknesses at $y = 0$, $\delta_z \simeq 2.85h$ (left) and $\delta_z \simeq h$ (right).

TURBULENT STATISTICS AND COHERENT STRUCTURES

After reviewing the most significant duct dynamics, and describing the complicated interactions taking place due to the presence of the side-walls (and essentially the inhomogeneity in the spanwise direction), we also compare the basic turbulent statistics of our computations with reference channel flow data (z-periodic). It is important to stress the fact that the local u_τ has to be used in order to scale the velocity profile at any particular z location, as opposed to the common practice of using the $\overline{u_\tau}$ value averaged over the duct width. If one wants to study the lo-

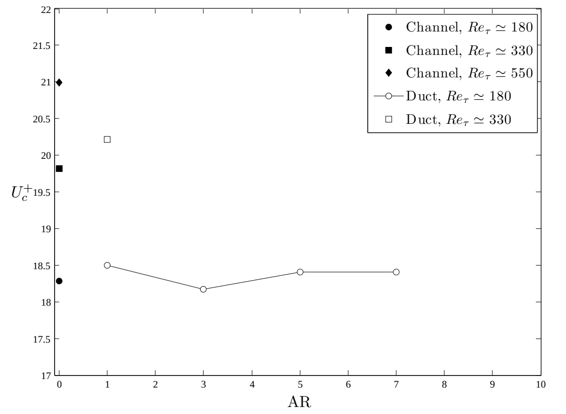

Figure 2. Inner-scaled centerline velocity U_c^+ as a function of aspect ratio for the DNSs of turbulent duct flow computed here, and reference channel flow DNSs (represented with aspect ratio 0) by del Álamo et al. (2004).

cal physics and interactions, the spanwise variation of wall shear also plays a role (very significant in the cases of turbulence intensity $\overline{u^2}^+$ and Reynolds shear stresses $\overline{uv}$). Figure 4 show the inner-scaled mean velocity profile U^+, streamwise and spanwise turbulence intensities $\overline{u^2}^+$ and $\overline{w^2}^+$, and Reynolds shear stress $\overline{uv}$, for the aspect ratio 3 case computed at $Re_{\tau,c} \simeq 180$ and the aspect ratio 1 at $Re_{\tau,c} \simeq 330$. This figure also shows the centerplane profile, as well as the spanwise variation and reference channel flow data from Moser et al. (1999) at nominal Re_τ values of 180 and 395.

For the square duct case, the mean flow progressively evolves with z towards a profile that is not far from the channel at the centerplane (although the κ values differ). The wall-normal velocity profile result of integrating the field in the spanwise direction significantly differs from the other two, especially as the centerline is approached, which is a consequence of the abrupt variations experienced in z. This effect is attenuated for higher aspect ratios since the wall shear distribution becomes more uniform throughout the width of the duct. With respect to the streamwise turbulence intensity, the centerplane of the duct exhibits a larger peak than the channel, but the most significant effect is the prominent peaks reached close to the centerline at spanwise locations half way between the wall and the core, $z \simeq \pm 0.5h$. These peaks exceed the centerplane peak values by a factor of 2. This effect is not observed in the spanwise turbulence intensity, and may be associated with elongated intermittent streamwise structures arising from the secondary vortices. These may also be connected with wall-normal shear transport, since this region is also characterized by positive values of the Reynolds shear stress $\overline{uv}$. Aspect ratio 3 coincidentally shows good agreement at the centerplane with the plane channel, although higher aspect ratio ducts start to depart again from the channel, especially when it comes to the peak values of the Reynolds stress tensor components (Vinuesa, 2013).

To conclude our analysis of aspect ratio effects on turbulent duct flows, we show some visualizations of coherent vortices in the flow. We consider the Q criterion Jeong and Hussain (1995) to define the structures, and Figure 5 shows the result for the aspect ratio 7 at $Re_{\tau,c} \simeq 180$ case. This figure first shows that the resolution considered for our computations was sufficient for the adequate characterization of the flow. In addition, Vinuesa (2013) shows that the coherent vortices are much more elongated than the equivalent structures found in turbulent channels (del Álamo et al., 2004), and the "forest" of structures is much less densely populated. The vortices attached to the side-walls also follow different dynamics than the ones from the channel, and further work at higher Reynolds numbers and aspect ratios is required for a complete characterization at a phenomenological level.

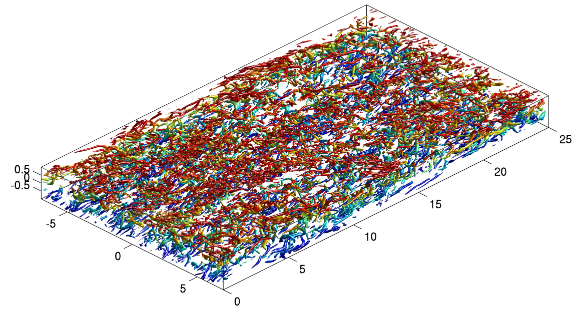

Figure 5. Coherent vortices defined using the Q criterion by Jeong and Hussain (1995) extracted from the aspect ratio 7 duct case at $Re_{\tau,c} \simeq 180$. Blue structures are closer to the lower walls, red structures to the upper one, and they get lighter as they approach to the core of the duct. Flow is from lower-left corner to upper-right.

SUMMARY AND CONCLUSIONS

Direct numerical simulations of turbulent duct flows with aspect ratios 1, 3, 5 and 7 with $Re_{\tau,c} \simeq 180$, and aspect ratio 1 at $Re_{\tau,c} \simeq 330$ have been carried out using three large supercomputing centers along the world. The highly scalable SEM code developed by Fischer *et al.* Fischer et al. (2008) was used, and high-efficiency MPI was also employed. The goal of these computations is to further understand experimental measurements of wall shear stress carried out at IIT (Vinuesa, 2013). The main conclusion is the fact that the flow at the core of a high aspect ratio (≥ 24) fully-developed ($x/H \simeq 200$) duct does not match the predictions from accurate DNSs of plane channel flows. The reason for this deviation is found in the three-dimensional effects present in the experimental duct and not captured by the z-periodic channel: secondary motions produced at the duct corner and side-wall boundary layers. These effects produce two energy flux mechanisms: energy is injected at the core of the duct due to the growth of the side-wall boundary layers, which accelerate this region. On the other hand, energy is extracted from this region due to the secondary motions that convect energy from the near-wall region to dissipate it at the corner bisectors. Thus, even if there is a region of nominally no spanwise velocity gradient at the duct core, the history effects play a role in how this state is reached, and it does not correspond to the plane channel results.

Analysis of the computational results and their evolution with aspect ratio lead to some interesting physical conclusions: as one increases the aspect ratio from 1 to 3, skin friction at the core of the duct also increases. However, if the aspect ratio is further increased to 5 or 7, skin friction decreases with aspect ratio. This is in agreement with the high aspect ratio experimental data (with AR from

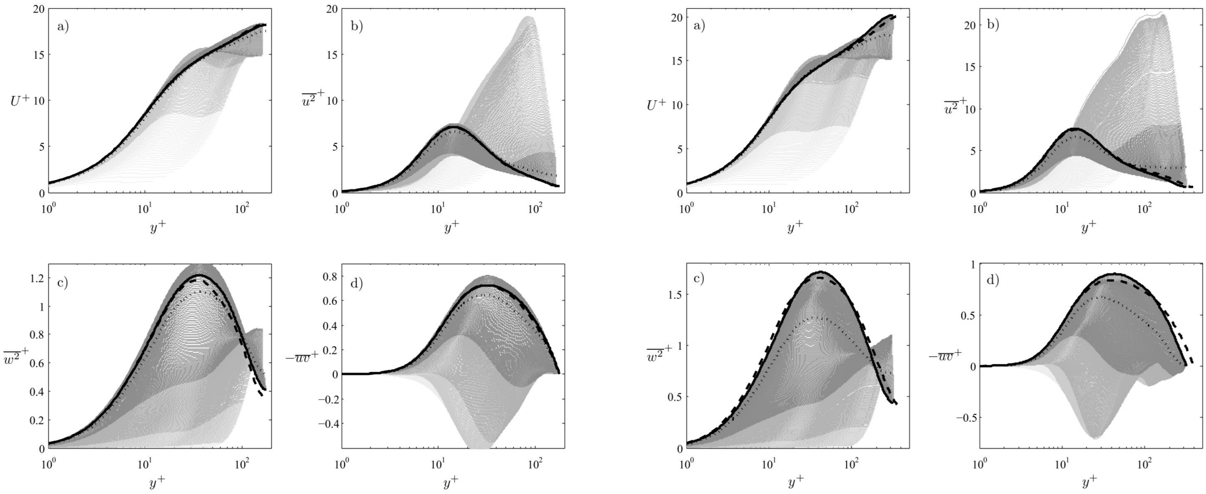

Figure 4. Aspect ratio 3 duct statistics at $Re_{\tau,c} \simeq 180$ (left) and aspect ratio 1 case at $Re_{\tau,c} \simeq 330$ (right). In both cases: a) mean flow, b) streamwise and c) spanwise turbulence intensities, and d) Reynolds shear stress. Inner scaling considering the local u_τ at each location, where lighter grey is associated with profiles close to the side-wall, whereas darker grey corresponds to flow closer to the core. Solid black corresponds to the duct profile at the centerplane, dashed black to the channel flow profiles by Moser et al. (1999) at $Re_\tau \simeq 180$ (left) and 395 (right), and dotted black is the wall-normal profile obtained after integration of the field in the spanwise direction.

12.8 to 48 by Vinuesa (2013)). This low-AR behavior can be explained in terms of the two three-dimensional effects: going from 1 to 3, the side-wall boundary layers significantly increase their size, leading to a much larger energy flux at the duct centerplane, which is not evacuated by the secondary motions. Larger aspect ratios lead to side-wall boundary layers with a uniform outer-scaled thickness of $\delta_z/w \simeq 0.85$, but increasing number of secondary vortices. This produces a negative energy balance at the duct core, which experiences an increased amount of energy being extracted by the secondary flow. These two phenomena can also be used to explain transient behavior in wall shear and centerline conditions, in terms of the unsteadiness of the secondary motions. An assessment of the presented data through comparisons with available computations and experiments in the literature highlights the high quality of the data.

REFERENCES

del Álamo, J. C., Jiménez, J., Zandonade, P., and Moser, R. D. (2004). Scaling of the energy spectra of turbulent channels. *J. Fluid Mech.*, 500:135–144.

Fischer, P. F., Kruse, J., Mullen, J., Tufo, H., Lottes, J., and Kerkemeier, S. (2008). Nek5000: Open source spectral element CFD solver. http://nek5000.mcs.anl.gov/index.php/MainPage.

Guala, M., Hommema, S. E., and Adrian, R. J. (2006). Large-scale and very-large-scale motions in turbulent pipe flow. *J. Fluid Mech.*, 554:521–542.

Huser, A. and Biringen, S. (1993). Direct numerical simulation of turbulent flow in a square duct. *J. Fluid Mech.*, 257:65–95.

Jeong, J. and Hussain, F. (1995). On the identification of a vortex. *J. Fluid Mech.*, 285:69–94.

Jiménez, J., del Álamo, J. C., and Flores, O. (2004). The large-scale dynamics of near-wall turbulence. *J. Fluid Mech.*, 505:179–199.

Jiménez, J. and Hoyas, S. (2010). Turbulent fluctuations above the buffer layer of wall-bounded flows. *J. Fluid Mech.*, 611:215–236.

Moinuddin, K. A. M., Joubert, P. N., and Chong, M. S. (2004). Experimental investigation of turbulence-driven secondary motion over a streamwise external corner. *J. Fluid Mech.*, 511:1–23.

Monty, J. P., Stewart, J. A., Williams, R. C., and Chong, M. S. (2007). Large-scale features in turbulent pipe and channel flows. *J. Fluid Mech.*, 589:147–156.

Moser, R. D., Kim, J., and Mansour, N. N. (1999). Direct numerical simulation of turbulent channel flow up to $Re_\tau = 590$. *Phys. Fluids*, 11(4):943–945.

Patera, A. T. (1984). A spectral element method for fluid dynamics: laminar flow in a channel expansion. *J. Comput. Phys.*, 54:468–488.

Pinelli, A., Uhlmann, M., Sekimoto, A., and Kawahara, G. (2009). Reynolds number dependence of mean flow structure in square duct turbulence. *J. Fluid Mech.*, 644:107–122.

Prandtl, L. (1926). Über die ausgebildete turbulenz. *Verh. 2nd Intl Kong. fur Tech. Mech., Zurich. English translation: NACA Tech. Memo*, 62:435.

Schlatter, P. and Örlü, R. (2012). Turbulent boundary layers at moderate reynolds numbers. Inflow length and tripping effects. *J. Fluid Mech.*, 710:5–34.

Uhlmann, M., Pinelli, A., Kawahara, G., and Sekimoto, A. (2007). Marginally turbulent flow in a square duct. *J. Fluid Mech.*, 588:153–162.

Vinuesa, R. (2013). *Synergetic computational and experimental studies of wall-bounded turbulent flows and their two-dimensionality*. PhD thesis, Illinois Institute of Technology, Chicago, USA.